symmetry

MDPI

Article

Transmission Properties of Electromagnetic Waves in Magneto-Electro-Elastic Piezoelectric Electromagnetic Metamaterials

Wen-Chao Bai [1,*], Hui Hu [1], Ben-Hu Zhou [1,*], Gui-Xiang Liu [1], Ge Tang [1], Yang-Yu Huang [1], Yan Cao [1], Han Zhang [2] and Han-Zhuang Zhang [2,*]

[1] Department of Physics, Shaoyang University, Shaoyang 422001, China
[2] Department of Physics, Jilin University, Changchun 130012, China
* Correspondence: 3569@hnsyu.edu.cn (W.-C.B.); 3473@hnsyu.edu.cn (B.-H.Z.); zhanghz@jlu.edu.cn (H.-Z.Z.)

Abstract: We designed magneto-electro-elastic piezoelectric, electromagnetic (EM) metamaterials (MEEPEM) by using a square lattice of the periodic arrays of conducting wires, piezoelectric photonic crystal (PPC), and split-ring resonators (SRRs). We analyzed the mechanism for multi-field coupling in MEEPEM. The magnetic field of the EM wave excites an attractive Ampère force in SRRs, which periodically compress MEEPEM, and this can create electric polarization due to the piezoelectric effect. The electric field of the EM wave can excite a longitudinal superlattice vibration in the PPC, which can also create electric polarization. The electric polarization can couple to the electric field of the periodic arrays of conducting wires. The coupled electric field will couple to the EM wave. These interactions result in multi-field coupling in MEEPEM. The coupling creates a type of polariton, called multi-field coupling polaritons, corresponding to a photonic band gap, namely, the multi-field coupling photonic band gap. We calculated the dielectric functions, the reflection coefficients, and the effective magnetic permeability of MEEPEM. By using them, we analyzed the transmission properties of EM waves in the MEEPEM. We analyzed the possibility of MEEPEM as left-handed metamaterials and zero refractive index material.

Keywords: metamaterials; magneto-electro-elastic materials; piezoelectric photonic crystal; split-ring resonators

check for updates

Citation: Bai, W.-C.; Hu, H.; Zhou, B.-H.; Liu, G.-X.; Tang, G.; Huang, Y.-Y.; Cao, Y.; Zhang, H.; Zhang, H.-Z. Transmission Properties of Electromagnetic Waves in Magneto-Electro-Elastic Piezoelectric Electromagnetic Metamaterials. *Symmetry* **2022**, *14*, 1942. https://doi.org/10.3390/sym14091942

Academic Editor: Marco Montemurro

Received: 10 August 2022
Accepted: 14 September 2022
Published: 18 September 2022

1. Introduction

Electromagnetic (EM) metamaterials, i.e., artificial composite structures created by the periodic arrays of conducting wires and split-ring resonators (SRRs), were shown to possess both negative permittivity and permeability frequency bands, creating a negative refraction index [1–6]. The EM metamaterials possess a number of peculiar properties, including inverse light pressure, a reverse Doppler effect, and opposite phase and energy velocities, which result in different capabilities for the manipulation of electromagnetic waves.

On the other hand, magneto-electro-elastic (MEE) materials have attracted exponentially increasing attention. The main reason behind this attention is that MEE structures can now convert electrical and magnetic energy due to the coupled effect between electric and magnetic fields. Because of this feature, MEE materials have been widely applied in many fields of modern technology, e.g., sensors [7], smart devices [8], and nondestructive evaluation [9]. Various analytical and numerical techniques related to various MEE structures have been developed by numerous scholars. Ezzin et al. [10] studied Love waves propagating in a transversely isotropic piezoelectric layer in a piezomagnetic half-space. Xiao et al. [11] investigated the dispersion characteristics of guided waves in a multilayered MEE curved panel. Chen et al. [12] investigated the dispersion and band structures of elastic waves in nanoscale periodic piezoelectric/piezomagnetic laminates. However, magneto-electro-elastic, piezoelectric, electromagnetic metamaterials (MEEPEM) have not been studied.

In this paper, we design the MEEPEM by using a square lattice of the periodic arrays of conducting wires, piezoelectric photonic crystals (PPC), and SRRs in Section 2. We analyze the mechanism for the coupling of the longitudinal superlattice vibrations, magnetic field, and electric field. We calculate the dielectric functions by using the Plane Wave Method, reflection coefficients by using the Transfer Matrix Method, and the effective magnetic permeability of MEEPEM. By using them, we will analyze the transmission properties of EM waves in the MEEPEM in Section 3. Conclusions are given in Section 4. We believe that our studies can contribute to the design of EM wave devices on the basis of the MEEPEM.

2. Dielectric Functions, Reflection Coefficients, and Effective Magnetic Permeability of MEEPEM

In order to elucidate the ideal of MEEPEM, we consider a composite structure consisting of a square lattice of the periodic arrays of conducting wires, PPCs, and SRRs shown schematically in Figure 1. In Figure 1a, for PPC, we choose ion-doped periodically poled lithium niobate crystal with the periodic concentration of the impurities in the positive and negative domains (IPPLN). The IPPLN can be produced by the Czochralski method [13–15], and the doping of ions does not change the symmetry of lithium niobate [16–18]. The ion-doped concentration of the IPPLN changes periodically; thus, the physical properties of IPLLN will be periodically changed. The ferroelectric domains of the IPPLN are periodically reversed along the *x* axis. We denote a and b as the thicknesses of positive and negative domains, respectively, and N_1 mol% and N_2 mol% ($N_1 \neq N_2$) as ion-doped concentrations in positive and negative domains, respectively. The period of domains is $\Lambda = a + b$, and the duty cycle is $r = a/b$. The thickness of the MEEPEM is b_0 along the *x* axis. The unit cell size of the MEEPEM is a_1. For simplicity, we choose the single-ring geometry of a lattice of cylindrical SRRs. The micro-structured material has been proposed and constructed to create left-handed metamaterials [19]. The SRRs are installed on the two surfaces of PPC along the *x* axis, and the directions of the gaps of the SRRs sharing a common axis are the same. The SRR can be equivalent to the *LC* oscillator with the capacitance *C* of the SRR gap, an effective inductance *L*, and resistance *R*. Figure 1b,c show the comparison of an equivalent *LC* circuit and a metallic SRR. The parameters of SRR are marked in Figure 1b: the gap size l_1, the thickness l_2, the width l_3, and the radius r_0. In Figure 1d, r_1 is the diameter of the conducting wire.

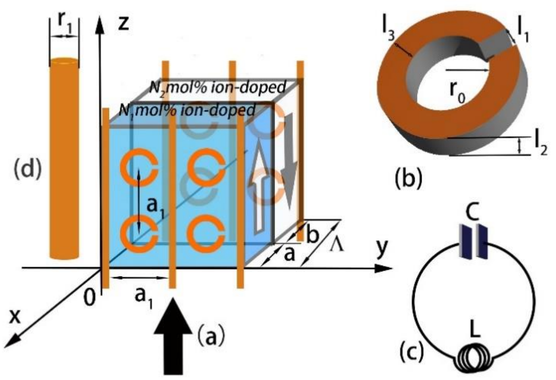

Figure 1. (**a**) A schematic diagram of MEEPEM, which is composed of a square lattice of the periodic arrays of conducting wires, PPC, and SRRs. Here, PPC is chosen as IPPLN, the positive and negative domains of which are arranged periodically along the *x* axis, and the arrows along the positive and negative *z* axes indicate the positive and negative domains, respectively. Here, only one period has been shown. The Mg concentrations in the positive and negative domains are N_1 mol% and N_2 mol% ($N_1 \neq N_2$), respectively. The bottom arrow indicates the direction of EM wave propagation. (**b**) SRR (with the gap size l_1, the thickness l_2, the width l_3, and the radius r_0). (**c**) SRR equivalent LC oscillator (with effective inductance *L* and the capacitance *C*). (**d**) r_1 is the diameter of the conducting wire.

As shown in Figure 1a, along the z axis, the EM waves with magnetic field H_x and electric field E_y propagate into MEEPEM. From Faraday's law of electromagnetic induction, magnetic field H_x will induce electric currents in identical SRRs sharing a common axis. In addition, the currents generate an attractive Ampère force between the SRRs, which compress PPC periodically. The Ampère forces acting between the SRRs have only the axial component, calculated as [20]:

$$F_i = \frac{\mu_0 b_0}{\gamma_0^2 \sqrt{4r_0^2 + b_0^2}} \left[\frac{2r_0^2 + b_0^2}{b_0^2} E - K \right] \left(\frac{\partial \phi}{\partial t} \right)^2, \tag{1}$$

where K is the complete elliptic integral of the first, E is that of the second kind, ϕ is magnetic flux, and

$$\gamma_0 = \sqrt{R^2 + \left[\omega L - \frac{1}{\omega C} \right]^2}, \tag{2}$$

where γ_0, $L = \mu_0 \pi r_0^2 / l_2$, and $C = \varepsilon_0 \varepsilon_C l_2 l_3 / l_1$ are the impedance, inductance, and capacitance of the SRR, respectively, and ε_C is the relative permittivity of the material filled in the SRR gap (see Figure 1b). We assume additional forces between the SRRs in the neighboring columns can be neglected. Because of the attractive Ampère forces between the SRRs, the stress can be calculated on the cross-sectional area of PPC along x axis, that is,

$$T_0 = \frac{m F_i}{S}, \tag{3}$$

where S is the cross-sectional area of the PPC along x axis, m is the number of SRRs, and T_0 is the periodic stress which is applied to the S of PPC. Because of the piezoelectric effect, the stress T_0 can generate transverse electric polarization. In response to the piezoelectric effect, the periodic electric field E_y of the EM wave can excite a longitudinal superlattice vibration. These will result in the coupling of electric, magnetic, and acoustic fields in the MEEPEM. The piezoelectric, Maxwell, and motion equations of the three field couplings are written as follows [21–23]:

$$T_1(x,t) + T_0 = C_{11}^E(x) S_1(x,t) + e_{22}(x) E_2(z,t), \tag{4}$$

$$D_2(z,t) = -e_{22}(x) S_1(x,t) - d_{22}(x) T_0 + \varepsilon_0 \varepsilon_{11}^S(x) E_2(z,t), \tag{5}$$

$$\frac{\partial^2 E_2(z,t)}{\partial z^2} = \mu_0 \frac{\partial^2 D_2(z,t)}{\partial t^2}, \tag{6}$$

$$\rho(x) \frac{\partial^2 S_1(x,t)}{\partial t^2} = \frac{\partial^2 T_1(x,t)}{\partial t^2}, \tag{7}$$

where

$$C_{11}^E(x) = \begin{cases} C_{11a}^E > 0 \text{ positive domain } (-\mathrm{a}/2 \le x \le \mathrm{a}/2) \\ C_{11b}^E > 0 \text{ negative domain } (-\Lambda/2 \le x < -a/2,\ a/2 < x \le \Lambda/2) \end{cases} \tag{8}$$

$$e_{22}(x) = \begin{cases} e_{22a} > 0 \text{ positive domain } (-\mathrm{a}/2 \le x \le \mathrm{a}/2) \\ -e_{22b} > 0 \text{ negative domain } (-\Lambda/2 \le x < -a/2,\ a/2 < x \le \Lambda/2) \end{cases} \tag{9}$$

$$d_{22}(x) = \begin{cases} d_{22a} > 0 \text{ positive domain } (-\mathrm{a}/2 \le x \le \mathrm{a}/2) \\ -d_{22b} > 0 \text{ negative domain } (-\Lambda/2 \le x < -a/2,\ a/2 < x \le \Lambda/2) \end{cases} \tag{10}$$

$$\varepsilon_{11}^S(x) = \begin{cases} \varepsilon_{11a}^S > 0 \text{ positive domain } (-\mathrm{a}/2 \le x \le \mathrm{a}/2) \\ \varepsilon_{11b}^S > 0 \text{ negative domain } (-\Lambda/2 \le x < -a/2,\ a/2 < x \le \Lambda/2) \end{cases} \tag{11}$$

$$\rho(x) = \begin{cases} \rho_a > 0 \text{ positive domain } (-\mathrm{a}/2 \le x \le \mathrm{a}/2) \\ \rho_b > 0 \text{ negative domain } (-\Lambda/2 \le x < -a/2,\ a/2 < x \le \Lambda/2) \end{cases} \tag{12}$$

where S_1, T_1, D_2, and E_2 are the strain, stress, electric displacement, and electric field, respectively, and they are functions of both position x and time t. $e_{22}(x)$, $d_{22}(x)$, $C_{11}^E(x)$, and $\varepsilon_{11}^S(x)$ are the piezoelectric stress, piezoelectric strain, elastic, and dielectric coefficients, respectively; $\rho(x)$ is the mass density of PPC, and they are periodic functions of position x. ε_0 is the permeability of the vacuum. Here, the damping of materials has been neglected.

Equation (3) implies the principle that the stress T_0 and E_y of EM wave create the longitudinal superlattice vibration S_1. Equation (4) implies the principle that the stress T_0 and longitudinal superlattice vibration S_1 can excite additional electric polarizations. Equations (3) and (4) imply the coupling of electric, magnetic, and acoustic fields due to the piezoelectric effect in the MEEPEM, resulting in a type of polariton, called the multi-field coupling polariton.

Substituting Equation (5) into Equation (6), we obtain:

$$T_0 = \frac{\varepsilon_0\left[\varepsilon_{11}^S(x) - 1\right]}{4d_{22}(x)} E_2(z,t) - \frac{e_{22}(x)S_1(x,t)}{4d_{22}(x)} S_1(x,t). \tag{13}$$

Substituting Equation (13) into Equation (4), we obtain:

$$T_1(x,t) = C'(x)S_1(x,t) + e'(x)E_2(z,t), \tag{14}$$

where the modulation functions $C'(x)$ and $e'(x)$ are expressed as follows:

$$C'(x) = \begin{cases} C'_a = C_{11a}^E - \frac{e_{22a}}{4d_{22a}} \text{ positive domain } \left(-\frac{a}{2} \le x \le \frac{a}{2}\right) \\ C'_b = C_{11b}^E - \frac{e_{22b}}{4d_{22b}} \text{ negative domain } \left(-\frac{\Lambda}{2} \le x < -\frac{a}{2}, \frac{a}{2} < x \le \frac{\Lambda}{2}\right) \end{cases}, \tag{15}$$

$$e'(x) = \begin{cases} e'_a = e_{22a} - \frac{\varepsilon_0\left[\varepsilon_{11a}^S - 1\right]}{4d_{22a}} \text{ positive domain } (-a/2 \le x \le a/2) \\ e'_b = e_{22b} - \frac{\varepsilon_0\left[\varepsilon_{11b}^S - 1\right]}{4d_{22b}} \text{ negative domain } (-\Lambda/2 \le x < -a/2,\ a/2 < x \le \Lambda/2) \end{cases}, \tag{16}$$

respectively. Using Fourier transformation, the modulation functions $C'(x)$ and $e'(x)$ are written as:

$$C'(x) = C_0 + \sum_{n \ne 0} C_n e^{iG_n x}, \tag{17}$$

$$e'(x) = e_0 + \sum_{n \ne 0} e_n e^{iG_n x}, \tag{18}$$

respectively, where $G_n = n\frac{2\pi}{\Lambda}$:

$$C_0 = \frac{C'_b + C'_a r}{r+1}, \tag{19}$$

$$e_0 = \frac{e'_a r - e'_b}{r+1}, \tag{20}$$

$$C_n = \left(C'_a - C'_b\right)\frac{1}{n\pi} sin\left(\frac{n\pi r}{1+r}\right), \tag{21}$$

$$e_n = \left(e'_a + e'_b\right)\frac{1}{n\pi}\sin\left(\frac{n\pi r}{1+r}\right). \tag{22}$$

Applying Equation (14) to Equation (7), we obtain:

$$S_1 = \sum_n \frac{e_n G_n^2 e^{iG_n x}}{\rho(x)\omega^2 - C'(x)G_n^2}. \tag{23}$$

Substitution of Equation (23) into Equation (5), we have:

$$D_2 = \varepsilon_0 \varepsilon_2(x,\omega) E_2, \tag{24}$$

where $\varepsilon_2(x,\omega)$ is the relative dielectric function:

$$\varepsilon_2(x,\omega) = \varepsilon_{11}^S(x) - \frac{1}{\varepsilon_0}\sum_n \frac{e_{22}(x)e_n G_n^2 e^{iG_n x}}{\rho(x)\omega^2 - C'(x)G_n^2} - \frac{d_{22}(x)}{\varepsilon_0}T_0^*, \quad (25)$$

where

$$T_0^* = \frac{m\mu_0^2\varepsilon_0\omega^2 S_0^2 b_0 E_2}{\gamma_0^2 S\sqrt{4r_0^2 + b_0^2}}\left[\frac{2r_0^2 + b_0^2}{b_0^2}E - K\right], \quad (26)$$

where $S_0 = \pi r_0^2$. The relative dielectric function $\varepsilon_2(x,\omega)$ is the function of the position x and angular frequency ω. We assume that the wavelength of an electromagnetic wave is larger than the unit cell size a_1 of the MEEPEM; then, the positive and negative domains of the MEEPEM can be considered homogeneous in space. With this approximation, the space average values are applicable, i.e., the positive domain $\varepsilon_{2a} = (1/a)\int_{-a/2}^{a/2}\varepsilon_2(x,\omega)dx$ and the negative domain $\varepsilon_{2b} = (1/b)[\int_{-\Lambda/2}^{-a/2}\varepsilon_2(x,\omega)dx + \int_{a/2}^{\Lambda/2}\varepsilon_2(x,\omega)dx]$. Then, the relative dielectric function of the positive domain is written as:

$$\varepsilon_{2a}(\omega) = \varepsilon_{11a}^S - \frac{4e_{22a}(e_a' + e_b')}{\varepsilon_0 a\Lambda\rho_a}\sum\nolimits_n \frac{\sin^2\left(\frac{n\pi r}{1+r}\right)}{\omega^2 - \omega_{an}^2} - \frac{d_{22a}}{\varepsilon_0}T_0^*, \quad (27)$$

where $\omega_{an} = C_a' G_n^2/\rho_a$ is the resonance angular frequency of the n-order multi-field coupling polariton of the positive domain. Furthermore, the relative dielectric function of the negative domain is written as:

$$\varepsilon_{2b}(\omega) = \varepsilon_{11b}^S - \frac{4e_{22b}(e_a' + e_b')}{\varepsilon_0 b\Lambda\rho_b}\sum\nolimits_n \frac{\sin^2\left(\frac{n\pi r}{1+r}\right)}{\omega^2 - \omega_{bn}^2} - \frac{d_{22b}}{\varepsilon_0}T_0^*, \quad (28)$$

where $\omega_{bn} = C_b' G_n^2/\rho_b$ is the resonance angular frequency of the n-order multi-field coupling polariton of the negative domain. For the unit cell of the periodic arrays of conducting wires, the average macroscopic electric field is approximately equal to the local field in the long-wavelength approximation. Taking into account Equations (27) and (28), and the effective dielectric permittivity of conducting wires [2], the expression for the relative dielectric function of the positive and negative domains of MEEPEM can be written as

$$\varepsilon_{ra} = \varepsilon_{2a}(\omega) - \frac{\omega_p}{\omega^2}, \quad (29)$$

and

$$\varepsilon_{rb} = \varepsilon_{2b}(\omega) - \frac{\omega_p^2}{\omega^2}, \quad (30)$$

respectively, where ω_p is the effective plasma frequency:

$$\omega_p^2 = \frac{2\pi c_0^2}{a_1^2\ln(2a_1/r_1)}, \quad (31)$$

where c_0 is the velocity of light in free space, and ω_p is the effective plasma frequency, r_1 is the diameter of the conducting wire, and a_1 is the unit cell size of the MEEPEM (see Figure 1).

On the basis of the Transfer Matrix Method of the photonic crystal and the relative dielectric functions ε_{ra} and ε_{rb} of MEEPEM [24–26], we calculate the reflection coefficients of the MEEPEM. It is derived as follows:

$$r = \frac{Z_1(M_{11} + Z_{N+1}M_{12}) - M_{21} - Z_{N+1}M_{22}}{Z_1(M_{11} + Z_{N+1}M_{12}) + M_{21} + Z_{N+1}M_{22}}, \quad (32)$$

where $Z_1 = n_1\sqrt{\varepsilon_0/\mu_0}$ (n_1 are the refractive indexes of the media before the EM waves propagate into the MEEPEM, μ_0 is the permeability of vacuum) and $Z_{N+1} = n_{N+1}\sqrt{\varepsilon_0/\mu_0}$ (n_{N+1} are the refractive indexes of the media after the EM waves propagate out of the MEEPEM) are the impedances of electromagnetic waves.

$$M = m^N = \begin{pmatrix} M_{11} & M_{12} \\ M_{21} & M_{22} \end{pmatrix}, \tag{33}$$

where

$$m = \begin{pmatrix} cos\beta_a cos\beta_b - \frac{n_b}{n_a} sin\beta_a sin\beta_b & -i\left(\frac{1}{Z_a} sin\beta_a cos\beta_b + \frac{1}{Z_b} cos\beta_a sin\beta_b\right) \\ -i(Z_b cos\beta_a sin\beta_b + Z_b sin\beta_a cos\beta_b) & cos\beta_a cos\beta_b - \frac{n_a}{n_b} sin\beta_a sin\beta_b \end{pmatrix}, \tag{34}$$

where $\beta_a = 2\pi n_a a/\lambda$, $\beta_b = 2\pi n_b b/\lambda$, $Z_a = n_a\sqrt{\varepsilon_0/\mu_0}$, and $Z_b = n_b\sqrt{\varepsilon_0/\mu_0}$. $n_a = \sqrt{\varepsilon_{ra}}$ and $n_b = \sqrt{\varepsilon_{rb}}$ are refractive indices of the positive domain and negative domain in MEEPEM, respectively.

In addition, a negative value of the magnetic permeability of the SRR in MEEPEM becomes possible (see Ref. [27]). According to the calculation method in the Refs. [1,27], we obtain an explicit expression for the effective magnetic permeability μ_{eff} of the composite structure in the long-wavelength approximation, that is,

$$\mu_{eff} = 1 - \frac{F\omega^2}{\omega^2 - \omega_{LC}^2 - \frac{jR\omega}{L}}, \tag{35}$$

where $\omega_{LC} = 1/\sqrt{LC}$ is the magnetic resonance angular frequency.

3. Results and Discussion

According to the relative dielectric function, effective magnetic permeability, and reflection coefficient, we can obtain the physical information required to study the transmission properties of EM waves in MEEPEM [1,21–27]. For the doped ion of IPPLN, we choose the Mg ion. The Mg ion concentrations of the positive and negative domains in MEEPEM are 0 mol% and 7 mol% [28] (see Figure 1), respectively. From Equations (27) and (28), the relative dielectric functions ε_{ra} and ε_{rb} of the first-order multi-field coupling polaritons in the MEEPEM are plotted in Figure 2. Because the damping of the material is not considered, Figure 2 shows only the real parts of the relative dielectric functions, and ε_{ra} and ε_{rb} are represented by the blue solid line and red dashed line, respectively. In this paper, the material parameters of the positive domain in MEEPEM are chosen from Ref. [21]: $C_{11a}^E = 2.03 \times 10^{11}$ N/m^2, e_{22a} = 2.50 C/m^2, $\rho_a = 4.700 \times 10^3$ kg/m^3, and ε_{11a}^S = 44.00. In addition, the proper values of the material parameters of the negative domain in MEEPEM are chosen as follows [28–32]: $C_{11b}^E = 3.00 \times 10^{11}$ N/m^2, e_{22b} = 2.32 C/m^2, $\rho_b = 4.630 \times 10^3$ kg/m^3, and ε_{11b}^S = 20.00. Other parameters include: the period Λ = 2 $\times 10^{-5}$ m, the number of the period N = 20, the duty cycle $r = a/b = 3$, m = 1, $r_0 = 2.0\times10^{-3}$ m, $S_0 = 1.26\times10^{-5}$ m^2, $S = 5.00\times10^{-5}$ m^2, the suitable values of the complete elliptic integrals of the first K and second kind E chosen from Refs. [33–35], E = 0.6, and K = 12.

Figures 3 and 4 show the high and low angular frequency regions of the dielectric spectrum in Figure 2, respectively. From Figure 3, the real parts of two dielectric functions ε_{ra} and ε_{rb} in the positive and negative domains exhibit negative values below angular frequencies $\omega_{p1} = 7.8\ Grad/s$ and $\omega_{p2} = 11.6\ Grad/s$, respectively. If we do not consider PPC and SRRs in the MEEPEM, the effective nonlinear dielectric permittivity of the periodic arrays of conducting wires is written as [2]:

$$\varepsilon_{eff} = 1 - \frac{\omega_p^2}{\omega^2}, \tag{36}$$

where ε_{eff} is the effective dielectric permittivity. From the above equation, we know $\varepsilon_{eff} < 0$ is below the effective plasma frequency ω_p = 51.5 Grad/s. Because of PPC and SRRs in the MEEPEM, the ω_p splits into two angular frequencies ω_{p1} and ω_{p2}, $\omega_{p1} < \omega_p$, and $\omega_{p2} < \omega_p$. At angular frequencies ω_{p1} and ω_{p2}, ε_{ra} = 0, and ε_{rb} = 0, correspond to two zero refractive indices. As shown in Figure 4, there are two dielectric abnormalities near the resonance angular frequencies ω_{a1} = 1.91 Grad/s and ω_{b1} = 1.95 Grad/s, corresponding to the first-order multi-field coupling polaritons for the coupled waves. The peaks of two dielectric abnormalities are greater than zero. At ω_{a1} and ω_{b1}, $\varepsilon_{ra} = 0$ and $\varepsilon_{rb} = 0$, correspond to two zero refractive indices.

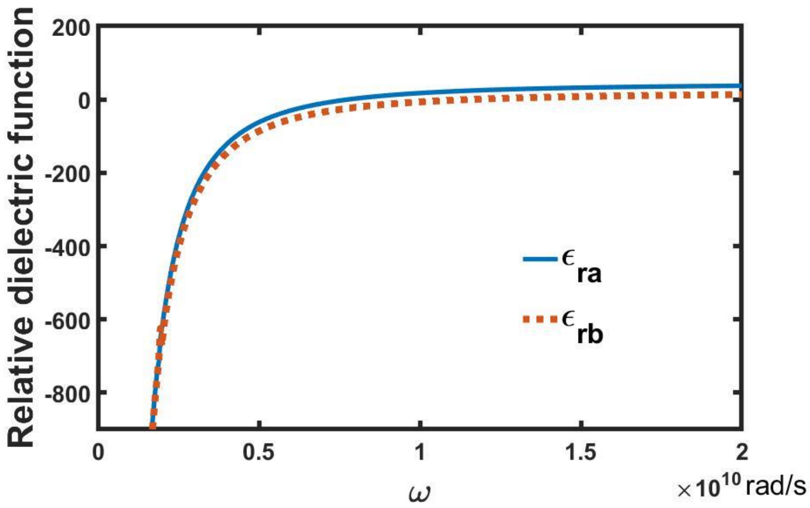

Figure 2. Schematics of the real parts of the relative dielectric functions $\varepsilon_{\mathrm{ra}}$ and $\varepsilon_{\mathrm{rb}}$, which are rep-resented by the blue solid line and red dashed line, respectively.

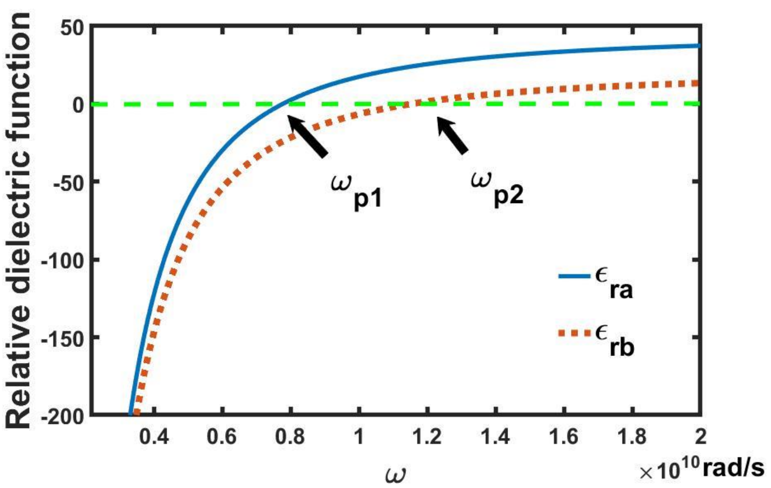

Figure 3. Relative dielectric functions ε_{ra} and ε_{rb} of MEEPEM in the high angular frequency re-gion, which are represented by the blue solid line and red dashed line, respectively. Because of PPC and SRRs in the MEEPEM, the effective plasma frequency ω_p conducting wires splits into two angular frequencies of ω_{p1} and ω_{p2}, $\omega_{p1} < \omega_p$ and $\omega_{p2} < \omega_p$.

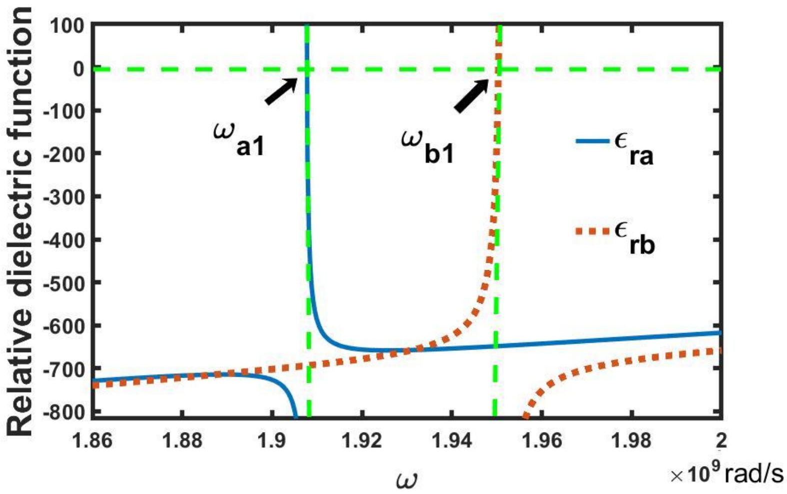

Figure 4. Relative dielectric functions $\varepsilon_{\rm ra}$ and $\varepsilon_{\rm rb}$ of MEEPEM in low angular frequency region, which are represented by the blue solid line and red dashed line, respectively. There are two dielec-tric abnormalities near the resonance angular frequencies ω_{a1} and ω_{b1} which are represented by the two green dashed lines in the vertical direction, corresponding to the first-order multi-field coupling polaritons for the coupled waves.

The results of the dielectric spectra in Figures 2–4 are interpreted as follows. Magnetic field H_x of the EM wave induces electric currents in two identical SRRs sharing a common axis, and the currents generate an attractive Ampère force between the SRRs, which periodically compress PPC, and this can create an additional electric polarization due to the piezoelectric effect. The electric field E_y of the EM wave can excite the longitudinal superlattice vibration in PPC, which can also create additional electric polarization. Two additional electric polarizations are coupled to the electric field excited by the periodic arrays of conducting wires. The coupled electric field is coupled to the EM wave along the z axis. These interactions result in the coupling between the longitudinal superlattice vibrations, magnetic field, and electric field in the MEEPEM, which cause variations in the dielectric spectrum. When the EM waves propagate along the x axis through the MEEPEM, it will be strongly reflected as long as its frequency lies in the angular frequency regions in which the dielectric function is negative. This is called the multi-field coupling photonic band gap (PBG).

In Figure 5, the entire reflection spectra of the MEEPEM and of the PPC are represented by the blue solid line and red dashed line, respectively. Here, the PPC is the IPPLN mentioned above. Figure 6 shows the cases in the low frequency region in Figure 5. In Figure 6, the reflection spectrum of the MEEPEM shows two reflection peaks and two zero reflection coefficients near the resonance angular frequencies ω_{a1} and ω_{b1} of the first-order multi-field coupling polaritons. Similar cases also exist in the reflection spectrum of the PPC. While the positions of two reflection peaks of PPC are higher than those of MEEPEM due to the resonant angular frequencies of PPC, they are higher than that of MEEPEM. In addition, the intensities of two reflection peaks of PPC are weaker than those of MEEPEM because the coupling of three fields in PPC is weaker than that of MEEPEM. We know the dielectric permittivity is a key factor in the calculation of the reflection coefficients. Therefore, the dielectric anomaly phenomena lead to the changes in the reflection spectra of the MEEPEM and PPC in Figure 6.

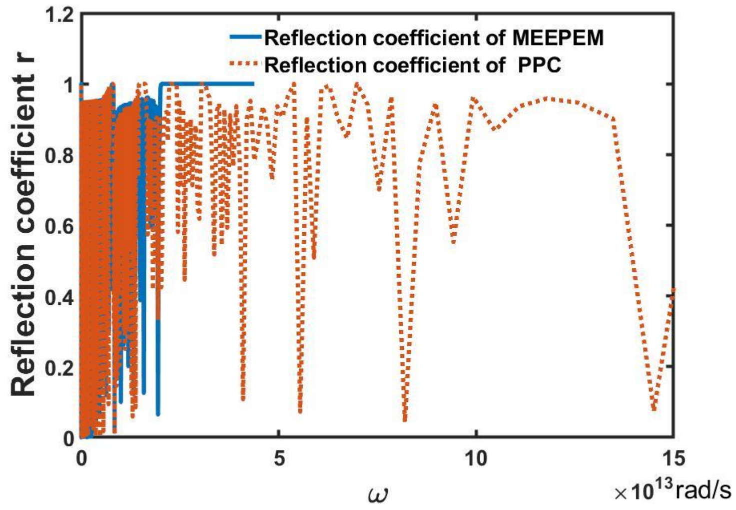

Figure 5. Comparison between the entire reflection spectrum of MEEPEM and that of PPC, which are represented by the blue solid line and red dashed line, respectively.

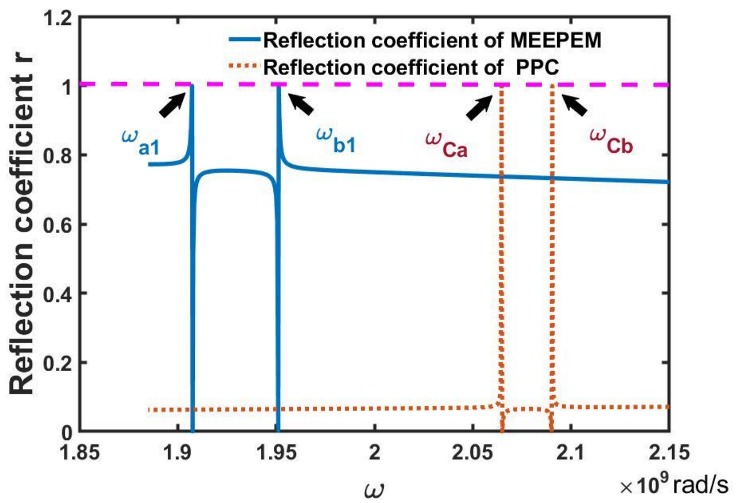

Figure 6. Reflection spectrums of MEEPEM and PPC in the low angular frequency region. Reflection spectra of MEEPEM and PPC are represented by the blue solid line and red dashed line, respectively. Near the resonance angular frequencies ω_{a1} and ω_{b1} of the first-order multi-field coupling polaritons, there are two reflection peaks and two zero reflection coefficients in the reflection spectrum of the MEEPEM, which also exist in the reflection spectrum of the PPC.

Figure 7 shows the cases in the high frequency region in Figure 5. As shown in Figure 7, the reflection spectrum of MEEPEM shows one very wide PBG, and that of PPC shows three PBGs (two of them are in the PBG of MEEPEM). The comparison is made in Table 1. The frequency position of MEEPEM is higher than that of PPC, and the frequency width of the PBG of the MEEPN is wider than the case of the PPC. The simulation results can be clarified by the variations in impedance Z_a and Z_b in Equation (32), which have a great influence on electromagnetic wave propagation. The impedance depends on the variation in the permittivity. Here, the variations in the permittivity are a result of the coupling between electric, acoustic, and magnetic fields in the MEEPEM. By fixing the values of other parameters in the Equation (32), we have investigated the effect of the dielectric permittivity on the PBGs. The research found the larger the ratio of ε_{2a} to ε_{2b}, the more the widths of the PBGs increase, and the higher the positions the PBGs move to, and vice versa.

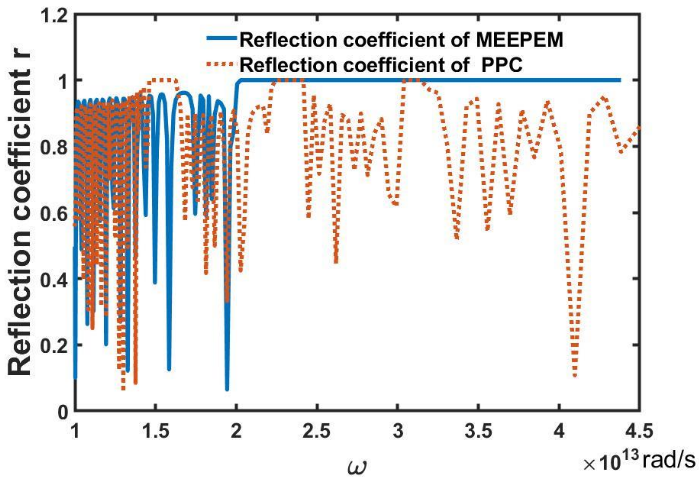

Figure 7. Reflection spectra of MEEPEM and PPC in high angular frequency region. Reflection spectra of MEEPEM and PPC are represented by the blue solid line and red dashed line, respectively. The reflection spectra of MEEPEM shows one very wide PBG, that of PPC shows three PBGs (two of them are in the PBG of MEEPEM).

Table 1. Comparison between PBGs of PPC and that of MEEPEM.

	Number of PBGs	**Width of PBG ($\times 10^{13}$ rad/s)**
PPC	three	0.164; 0.173; 0.102 [1]
MEEPEM	one	2.357

[1] From left to right in Figure 7.

From Equation (33), the real part of the effective magnetic permeability function μ_{eff} of SRR is shown in Figure 8, which is represented by the blue solid lines; here, $l_1 = 1 \times 10^{-7}$m, $l_2 = 1 \times 10^{-6}$m, and $l_3 = 1 \times 10^{-4}$m. As can be seen in Figure 8, there is one anomalous peak near the magnetic resonance angular frequency ω_{LC} = 2.68 Grad/s. The effective magnetic permeability μ_{eff} exhibits negative values in the angular frequency gap (ω_{LC}, ω_{LCP}), i.e., PBG, in which the propagation of EM waves in MEEPEM will be forbidden, where ω_{LCP} = 2.70 Grad/s, which can be obtained by setting μ_{eff} = 0 in Equation (33). Upon inserting ω_{LCP} in the expression $\omega_{LCP} - \omega_{LC}$, we can obtain the width of the PBG. While in the PBG (ω_{LC}, ω_{LCP}), the real parts of two dielectric functions ε_{ra} and ε_{rb} also exhibit negative values. That is, both the magnetic permeability and dielectric permittivity of the MEEPEM are negative, and the MEEPEM will become the left-handed metamaterial with negative refraction [2,36–39]. In the MEEPEM, the condition for obtaining a negative refractive index is ω_{LCP} < min (ω_{p1}, ω_{p2}), which can be obtained by adjusting the structural parameters of the SRRs in MEEPEM.

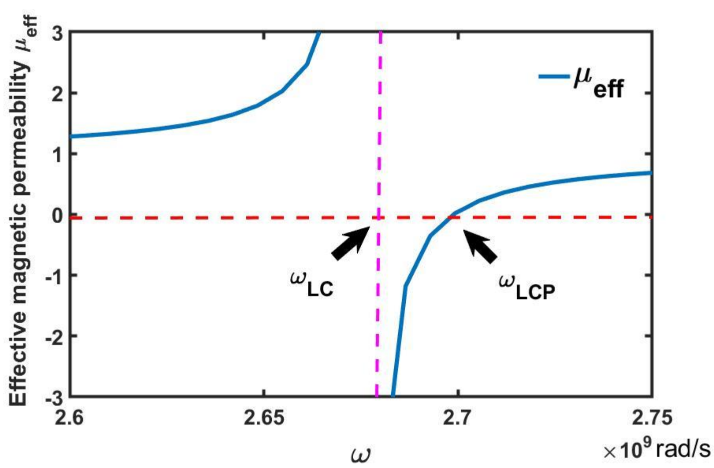

Figure 8. Effective magnetic permeability function μ_{eff} for the SRRs which is represented by the blue solid lines. There is one anomalous peak near the magnetic resonance frequency ω_{LC} which is represented by the pink dashed line in the vertical direction. The μ_{eff} exhibits negative values in the PBG (ω_{LC}, ω_{LCP}), where the EM wave propagation will be forbidden.

4. Conclusions

In summary, we have designed an MEEPEM with a square lattice of the periodic arrays of conducting wires, PPC, and SRRs. We analyzed the mechanism for multi-field coupling in MEEPEM. The magnetic field of the EM wave excites an attractive Ampère force in two identical SRRs sharing a common axis, which periodically compress PPC, and this can create additional electric polarization due to the piezoelectric effect. While the electric field of the EM wave can excite longitudinal superlattice vibration in the PPC, it can also create additional electric polarization. Two additional electric polarizations are coupled to the electric field of the periodic arrays of conducting wires. The coupled electric field is coupled to the EM wave. These interactions result in the coupling between the longitudinal superlattice vibrations, magnetic field, and electric field in the MEEPEM.

We have calculated the dielectric functions, the effective magnetic permeability, and the reflection coefficients of MEEPEM. By using them, we have analyzed the transmission properties of EM waves in the MEEPEM. From the dielectric spectrum, we found the effective plasma frequency of conducting wires splits into two angular frequencies. Near the resonance angular frequencies of multi-field coupling polaritons, there are two dielectric abnormalities. The negative regions of the dielectric spectrum form PBGs. In addition, the dielectric spectrum exhibits four frequency positions of zero refractive indices. According to the reflection spectrum, near the resonance angular frequencies of multi-field coupling polaritons, there are two reflection peaks of both MEEPEM and PPC. The positions and intensities of two reflection peaks of PPC are higher and weaker than those of MEEPEM, respectively. In addition to these, the reflection spectrum of MEEPEM shows one very wide PBG, and that of PPC shows three PBGs (two of them are in the PBG of MEEPEM). The PBG position of MEEPEM is higher that of PPC, and the PBG width of MEEPN is wider than the case of the PPC. The variations in these properties are a result of the coupling between the longitudinal superlattice vibrations, magnetic field, and electric field in the MEEPEM.

The effective magnetic permeability also exhibits one PBG near the magnetic resonance angular frequency. By adjusting the structure parameters of the SRRs in MEEPEM, if PBG of effective magnetic permeability exists in the range of the PBGs of the dielectric function, the MEEPEM will become a left-handed metamaterial with negative refraction.

Furthermore, by modulating the MEEPEM parameters, the MEEPEM can meet the application requirements. These basic theoretical studies provide guidance for the application of MEEPEM in the field of electromagnetic waves, such as the polarizer, the reflector, and wavelength division multiplexing devices.

Author Contributions: W.-C.B.: Ideas; formulation or evolution of overarching research goals and aims; management and coordination responsibility for the research activity planning and execution; designing computer programs; development or design of methodology. H.H.: Development or design of methodology; creation of models; designing computer programs. B.-H.Z.: Application of statistical, mathematical, computational, or other formal techniques to analyze or synthesize study data. G.-X.L.: Preparation, creation, and/or presentation of the published work, specifically writing the initial draft (including substantive translation). G.T. and Y.-Y.H.: Preparation, creation, and presentation of the published work, specifically writing the initial draft (including substantive translation). Y.C.: Conducting the research and investigation process and data collection. H.Z.: Conducting the research and investigation process, data collection, programming. H.-Z.Z.: Provision of study materials; management and coordination responsibility for the research activity planning and execution. All authors have read and agreed to the published version of the manuscript.

Funding: This work is supported by the Hunan Provincial Natural Science Foundation of China (Grant No. 2020JJ4555) and the Natural Science Foundation of Hunan Province of China (Grant No. 2022jj50180).

Data Availability Statement: Not applicable.

Conflicts of Interest: We declare that we have no financial and personal relationships with other people or organizations that can inappropriately influence our work; there is no professional or other personal interest of any nature or kind in any product, service or company that could be construed as influencing the position presented in, or the review of, the manuscript entitled "Transmission Properties of Electromagnetic Waves in Magneto-Electro-Elastic Piezoelectric Electromagnetic Metamaterials".

References

1. Pendry, J.B.; Holden, A.J.; Robbins, D.J.; Stewart, W.J. Magnetism from conductors and enhanced nonlinear phenomena. *IEEE Trans. Microw. Theory Tech.* **1999**, *47*, 2075–2084. [CrossRef]
2. Pendry, J.B.; Holden, A.J.; Stewart, W.J.; Youngs, I. Extremely low frequency plasmons in metallic meso-structures. *Phys. Rev. Lett.* **2001**, *87*, 4773–4776.
3. Abdulkarim, Y.I.; Özkan Alkurt, F.; Awl, H.N.; Altıntaş, O.; Muhammadsharif, F.F.; Appasani, B.; Bakır, M.; Karaaslan, M.; Taouzari, M.; Dong, J. A Symmetrical Terahertz Triple-Band Metamaterial Absorber Using a Four-Capacitance Loaded Complementary Circular Split Ring Resonator and an Ultra-Thin ZnSe Substrate. *Symmetry* **2022**, *14*, 1477. [CrossRef]
4. Lv, Z.; Li, Z.; Han, Y.; Cao, Y.; Yang, L. A Wideband and Ultra-Thin Metamaterial Absorber Based on Resistive FSS. *Symmetry* **2022**, *14*, 1148. [CrossRef]
5. Liu, N.; Lei, X.; Lai, F.; Xue, X. Longitudinal Wave Locally Resonant Band Gaps in Metamaterial-Based Elastic Rods Comprising Multi-Degree-of-Freedom DAVI Resonators. *Symmetry* **2022**, *14*, 1030. [CrossRef]
6. Kim, Y.; Lee, J.-H. Design of Broadband and Wide-Angle Hexagonal Metamaterial Absorber Based on Optimal Tiling of Rhombus Carbon Pixels and Implantation of Copper Cylinders. *Symmetry* **2021**, *13*, 2045. [CrossRef]
7. Tiercelin, N.; Dusch, Y.; Preobrazhensky, V.; Pernod, P. Magnetoelectric memory using orthogonal magnetization states and magnetoelastic switching. *J. Appl. Phys.* **2011**, *109*, 726. [CrossRef]
8. Fiebig, M. Revival of the magnetoelectric effect. *J. Phys. D Appl. Phys.* **2005**, *38*, 123. [CrossRef]
9. Achenbach, J.D. Quantitative nondestructive evaluation. *Int. J. Solids Struct.* **2000**, *37*, 13–27. [CrossRef]
10. Ezzin, H.; Amor, M.B.; Ghozlen, M.H.B. Love waves propagation in a transversely isotropic piezoelectric layer on a piezomagnetic half-space. *Ultrasonics* **2016**, *69*, 83–89. [CrossRef]
11. Xiao, D.L.; Han, Q.; Jiang, T.J. Guided wave propagation in a multilayered magneto-electro-elastic curved panel by Chebyshev spectral elements method. *Compos. Struct.* **2019**, *207*, 701–710. [CrossRef]
12. Chen, A.L.; Yan, D.J.; Wang, Y.S.; Zhang, C.Z. In-plane elastic wave propagation in nanoscale periodic piezoelectric/piezomagnetic laminates. *Int. J. Mech. Sci.* **2019**, *153*, 416–429. [CrossRef]
13. Tasson, M.; Legal, H.; Gay, J.S.; Peuzin, J.C.; Lissalde, F.S. Piezoelectric study of poling mechanism in lithium niobate crystals at temperature close to the curie point. *Ferroelectrics* **1976**, *13*, 479–481. [CrossRef]
14. Magel, G.A.; Fejer, M.M.; Byer, R.L. Quasi-phase-matched second-harmonic generation of blue light in periodically poled $LiNbO_3$. *Appl. Phys. Lett.* **1990**, *56*, 108–110. [CrossRef]
15. Evlanova, I.I.N.N.F.; Gliko, O.A.; Lavrishchev, S.V. Study of periodically poled Czochralski-grown Nd:Mg:$LiNbO_3$ by chemical etching and X-ray microanalysis. *J. Cryst. Growth* **1991**, *181*, 160–164.
16. Hammoum, R.; Fontana, M.D.; Gilliot, M.; Bourson, P.; Kokanyan, E.P. Site spectroscopy of Hf doping in Hf-doped $LiNbO_3$ crystals. *Solid State Commun.* **2009**, *149*, 1967. [CrossRef]
17. Lorenzo, A.; Jaffrezic, H.; Roux, B.; Boulon, G.; Garcia-Sole, J. Lattice location of rare-earth ions in $LiNbO_3$. *Appl. Phys. Lett.* **1995**, *67*, 3735. [CrossRef]

18. Donnerberg, H.; Tomlinson, S.M.; Catlow, C.R.A.; Schirmer, O.F. Computer-simulation studies of extrinsic defects in $LiNbO_3$ crystals. *Phys. Rev. B* **1991**, *44*, 4877. [CrossRef]
19. Smith, D.R.; Padilla, W.J.; Vier, D.C.; Nemat-Nasser, S.C.; Schultz, S. Composite medium with simultaneously negative permeability and permittivity. *Phys. Rev. Lett.* **2000**, *84*, 4184. [CrossRef]
20. Landau, L.D.; Lifschitz, E.M. *Electrodynamics of Continuous Media*; Pergamon Press: Oxford, UK, 1984.
21. Auld, B.A. *Acoustic Fields and Waves in Solids*; Wiley: New York, NY, USA, 1973.
22. Bai, W.C.; Lan, Z.J.; Zhang, H.; Jiang, L. Theoretical investigation of the phonon-polaritonmode in Czochralski grown piezoelectric superlattice. *Superlattices Microstruct.* **2016**, *97*, 167–175. [CrossRef]
23. Bai, W.C.; Zhang, H.; Jiang, L.; Zhang, H.Z.; Zhang, L.Q. Theoretical investigation of phonon-polariton modes in undoped and ion-doped PPLN crystals. *Solid State Commun.* **2011**, *151*, 1261–1265. [CrossRef]
24. Winn, J.N.; Fink, Y.; Fan, S.; Joannopoulos, J.D. Omnidirectional reflection from a one-dimensional photonic crystal. *Opt. Lett.* **1998**, *23*, 1573–1575. [CrossRef] [PubMed]
25. Brakat, O. Theoretical investigation of transmission and dispersion properties of one dimensional photonic crystal. *J. Electr. Electron. Eng.* **2015**, *3*, 12–18. [CrossRef]
26. Pendry, J.B.; Mackinnon, A. Calculation of photon dispersion. *Phys. Rev. Lett.* **1992**, *69*, 2772–2775. [CrossRef] [PubMed]
27. Zharov, A.A.; Shadrivov, I.V.; Kivshar, Y.S. Nonlinear properties of left-handed metamaterials. *Phys. Rev. Lett.* **2003**, *91*, 037401. [CrossRef] [PubMed]
28. Bai, W.C.; Jiang, L.; Zhang, H.Z.; Ma, G.H. Influence of Mg doping on the dielectric properties of MgO-doped lithium niobate. *Phys. B* **2011**, *406*, 1567. [CrossRef]
29. Kushibiki, J.; Kobayashi, T.; Ishiji, H.; Chubachi, N. Elastic properties of 5 mol% MgO doped $LiNbO_3$ crystals measured by line focus beam acoustic microscopy. *Appl. Phys. Lett.* **1992**, *61*, 2164–2166. [CrossRef]
30. Xue, D.F.; He, X.K. Dopant occupancy and structural stability of doped lithium niobate crystals. *Phys. Rev. B* **2006**, *73*, 064113. [CrossRef]
31. Kushibiki, J.; Kobayashi, T.; Ishiji, H.; Jen, C.K. Surface-acoustic-wave properties of MgO-doped $LiNbO_3$ single crystals measured by line-focus-beam acoustic microscopy. *J. Appl. Phys.* **1999**, *85*, 7863. [CrossRef]
32. Xue, D.; Kitamura, K. Dielectric characterization of the defect concentration in lithium niobate single crystals. *Solid State Commun.* **2002**, *122*, 537. [CrossRef]
33. Qi, F.; Zhang, H. Inequalities of the complete elliptic integrals. *Tamkang J. Math.* **1995**, *3*, 165–169. [CrossRef]
34. Cerone, P.; Dragomir, S.S. Lobatto type quadrature rules for functions with bounded derivative. *Math. Inequal Appl.* **2003**, *3*, 197–209. [CrossRef]
35. Guo, B.N.; Feng, Q. Some bounds for the complete elliptic integrals of the first and the second kinds. *Math. CA* **2009**, *18*, 2787–2790. [CrossRef]
36. Veselago, V.G.; Lebedev, P.N. The electrodynamics of substances with simultaneously negative values of ε and μ. *Sov. Phys. Usp.* **1968**, *10*, 509–514. [CrossRef]
37. Parazzoli, C.G.; Greegor, R.B.; Li, K.; Koltenbah, B.E.C.; Tanielian, M. Experimental verification and simulation of negative index of refraction using Snell's law. *Phys. Rev. Lett.* **2003**, *90*, 107401. [CrossRef] [PubMed]
38. Ullah, M.H.; Uddin, M.J.; Latef, T.A.; Mahadi, W.N.L.; Ahsan, M.R.; Islam, M.T. Constitutive parameter analysis of left-handed dual-star split-ring resonator metamaterial for homogeneous infinite slab. *IET Microw. Antennas Propag.* **2015**, *9*, 1740–1746. [CrossRef]
39. Uddin, M.J.; Ullah, M.H.; Latef, T.A.; Mahadi, W.N.L. Inversion response to optimize lumped-element circuits for metamaterial. *Int. J. Circ. Theor. Appl.* **2017**, *45*, 36–46. [CrossRef]